

Article

Adaptive Feedforward Control Based on Estimated Electromagnetic Parameters upon a Novel Two-Degrees-of-Freedom Actuator with a Unibody Magnetic Circuit

Zhaoxi Yi ¹, Meizhu Luo ^{1,*} , Ji-an Duan ¹ and Yan Jiang ²

¹ College of Mechanical and Electrical Engineering, Central South University, Changsha 410083, China; yizhaoxi_academy@163.com (Z.Y.); xinruoliuli.07@163.com (J.-a.D.)

² College of Electrical and Information Engineering, Hunan University, Changsha 410082, China; yaj@hnu.edu.cn

* Correspondence: luomz2019@csu.edu.cn

Abstract: This paper focuses on the study of the tracking performance of a novel two-degrees-of-freedom (two-DOF) voice coil motor (VCM). Intelligent control algorithms estimate the motor control model by the relationship between the input and output values, and it is hard to achieve excellent tracking performance due to the wider variational range of motor electromagnetic parameters (MEPs). This paper proposes estimated methods for MEPs and an adaptive feedforward control algorithm based on estimated MEPs (ACBE). ACBE can alter its control parameters from inside out in time with the change in MEPs. Experiments are carried out to verify that the proposed ACBE realized excellent tracking performance upon the novel two-DOF VCM. This study indicates that an adaptive control algorithm with high-precision control parameters has better tracking performance upon a motor control model with large variation.

Keywords: fitted adaptive fuzzy controller (FAFC); linear motor servo system; tracking performance



Citation: Yi, Z.; Luo, M.; Duan, J.-a.; Jiang, Y. Adaptive Feedforward Control Based on Estimated Electromagnetic Parameters upon a Novel Two-Degrees-of-Freedom Actuator with a Unibody Magnetic Circuit. *Energies* **2024**, *17*, 3017. <https://doi.org/10.3390/en17123017>

Academic Editor: Andrea Mariscotti

Received: 13 April 2024

Revised: 17 June 2024

Accepted: 17 June 2024

Published: 19 June 2024



Copyright: © 2024 by the authors. Licensee MDPI, Basel, Switzerland. This article is an open access article distributed under the terms and conditions of the Creative Commons Attribution (CC BY) license (<https://creativecommons.org/licenses/by/4.0/>).

1. Introduction

This paper focuses on the study of the tracking performance of a novel two-DOF VCM, which is applied as an end-effector of an optical fiber alignment system. The end-effectors of high-performance multi-dimensional motion platforms directly act on their terminal properties [1–3]. In order to improve the precision and reduce equipment size, multi-degrees-of-freedom motors are potential force sources for these end-effectors [4,5]. The novel two-DOF VCM has the advantage of a higher power–mass ratio and lower thrust (torque) ripple [6]. The structure of this novel two-DOF VCM is shown in Figure 1. Its linear mover and rotary rotor share one stator; this stator employs one permanent magnet (PM) to excite the main magnetic field, and the PM is magnetized in the direction of y . A Lorentz force will act on the linear coil of this two-DOF VCM when current flows through it; then, a linear reciprocating motion along direction x is produced. A Lorentz force also will be imposed on the rotary coil when current flows through it, but a rotary motion around the axis of the precision bearing is generated due to the special mechanism of the rotary coil and its bracket. The peculiarities of this novel two-DOF VCM are as follows:

- (1) The linear coil and swing coil share one iron yoke; their main magnetic circuits are the same. When the current in one coil changes, a related electromotive force (EMF) will be induced by the other coil.
- (2) Due to the rotation of the rotor, the relative position of the linear coil and the rotary coil will change; this leads to variations in the mutual inductance between the two coils and the leakage inductance of the rotary coil.

- (3) The swing coil also has back EMF when the linear motion is active separately.

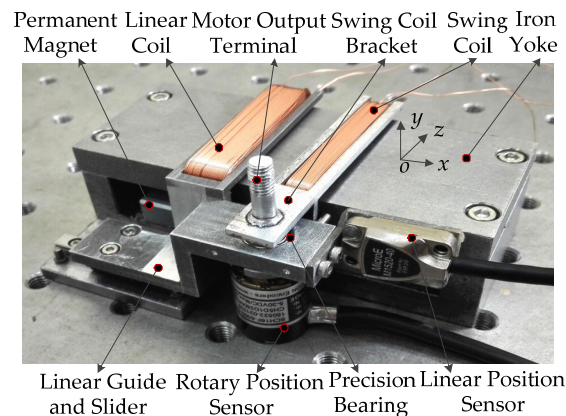


Figure 1. Structure of the novel two-DOF VCM.

The novel two-DOF VCM will carry optical fibers and scan for a light source. Excellent position tracking control performance is helpful for improving the quality and efficiency of fiber alignment. Many control strategies are used to improve the accuracy and tracking performance of motion systems. In [7], fuzzy control was adopted to achieve 15% speed tracking error upon a butterfly-shaped linear ultrasonic motor. To deal with the hysteresis of piezoelectric actuators, a fuzzy adaptive internal model controller was designed to improve the tracking performance, and 0.32% tracking error was realized [8]. Further, Long Cheng provided an adaptive fuzzy model-based predictive controller for piezoelectric actuators and reduced the tracking error to 0.2% [9]. Fuzzy fractional-order sliding-mode control effectively attenuated the chattering upon a permanent magnet linear synchronous motor and realized 0.26% tracking error [10].

Pan Huihui proposed disturbance observer-based adaptive tracking control for a class of nonlinear systems with parametric uncertainty, bounded external disturbance, and actuator saturation. The modeling inaccuracy and disturbance were integrated by a disturbance observer, which was estimated and compensated [11]. Liu Xiufeng took position and velocity as variates to establish a linear extended state observer for an iron-less permanent magnet linear synchronous motor. The precision control could compensate the slow-varying disturbance due to the observer, and 1.5 μm tracking performance was obtained [12]. Further, a periodic adaptive disturbance observer was provided for a permanent magnet linear synchronous motor, which estimated parametric errors, friction force, and force ripple. Depending on the observer, a 2.7 μm tracking performance was realized [13]. Zhao Ling designed observer-based integral sliding-mode tracking control for a pneumatic cylinder with varying loads. The generalized nonlinear extended state observer estimated the total disturbance and its derivative for the system, which reduced the tracking error to 0.25 mm [14]. An internal model control PID method based on a model linear extended state observer was used to improve the estimation accuracy for the system states and total unknown uncertainties, which was applied to a permanent magnet linear synchronous motor servo system, and 0.18% tracking error was accomplished [15]. An improved sliding-mode observer was also presented, which was based on the design idea of “identification–adjustment–adaptation”. It could adaptively estimate the load torque during variable-speed and variable-load operation and improved the response to load change successfully [16].

Active disturbance rejection control (ADRC) is an effective method for precision motion. In [17], a particle swarm optimization method was suggested to tune the parameters of ADRC for a magnetic levitation system, which enhanced the dynamic performance of the control system. The control strategy had better disturbance rejection capability. Predictive control is another control strategy for precision motion systems. Model predictive control was provided for a three-phase permanent magnet synchronous motor to deal

with parameter variation and improve control precision, which was based on an indirect reference vector with an extended control set, and 8.9% current total harmonic distortion was realized [18]. Further, recurrent-neural-network-based model predictive control was presented for a nano-positioning system. The nonlinear dynamics of the nano-positioning system were accurately captured, which effectively guarantees the track performance of the system [19]. Xu Qingsong provided digital integral terminal sliding-mode predictive control for a piezoelectric-driven motion system. The control strategy was output-based and did not require a hysteresis model and a state observer and achieved 0.16% tracking performance [20].

The traditional identification methods of motor parameters include the Kalman filter [21,22], least square method [23,24], etc. The Kalman filter algorithm involves a lot of matrix and vector operations and needs to pre-process the motor mathematical model, so the process is complicated. The least square method needs to calculate the derivative of the objective function with respect to the motor parameters, which is susceptible to interference from measurement noise and motor speed fluctuations, which means unsteadiness. Compared with traditional methods, the intelligent optimization algorithm has the advantages of high efficiency, strong robustness, and low requirements for the objective function, such as the neural network algorithm [25,26]. However, it still has some problems, such as weak global search ability, poor anti-interference ability, and slow convergence speed.

Adaptive fuzzy control does not require an exact control model and has the advantages of stronger robustness and better tracking performance, but the fuzzy rule is key in precision motion and hard to obtain. The observer establishes equations of state from inputs and outputs and identifies the changes in the control model. However, the performance of the observer in one control system depends on precise state equations, which are non-universal and need be gradually optimized by lots of test data. The effect of ADRC and predictive control essentially depends on the accuracy of their control parameters, which are given by another intelligent algorithm. Nevertheless, the applicable intelligent algorithm also needs to be optimized by lots of data or be deduced by complex mathematical models.

Some of the above-discussed control algorithms require a lot of data, such as fuzzy control and neural networks; some are limited by the compensation accuracy of the inverter, such as the state observer; and some require a lot of computational time, such as the least squares method. At the same time, the control algorithms discussed above do not consider the characteristics of the control object, which is not conducive to the further optimization of the control performance. Based on the structure of the novel two-DOF VCM, this paper proposes a real-time estimated method for MEPs to deal with their changefulness. The estimated MEPs include the electrical time constant, torque/thrust constant, and back-EMF constant. The estimated method of the electrical time constant is based on the estimation of armature inductance, which is elaborated in Section 2. The estimated method of the torque/thrust constant and back-EMF constant is based on the estimation of air-gap flux density, which is elaborated in Section 3. This paper also proposes an adaptive feedforward control algorithm from inside out based on estimated parameters (ACBE) in Section 4. ACBE does not require measured data for optimization or complex control rules, and the control performance of ACBE depends mainly on the accuracy of the estimated electromagnetic parameters. Section 5 provides the experimental verification and analysis. The conclusion is given in Section 6.

2. Estimated Method of Electrical Time Constant

The estimated method of the electrical time constant in this paper takes core-loss resistance and magnetizing inductance as constant and time-varying parameters, respectively, in one current cycle. When the swing motion is active, the linear coil is treated as the tested coil, and the equivalent circuit of the swing motion is shown in Figure 2. R_1 and $L_{1\sigma}(\theta)$ are the resistance and leakage inductance of the swing coil, respectively, $M_{12\sigma}(\theta)$ is the mutual inductance between the swing and linear coil, $u_{e\omega}(t)$ and θ are the back EMF and angle of swing motion, respectively, $u_1(t)$ and $i_1(t)$ are the voltage and current of the

swing coil, respectively, N_1 and N_2 are the turns of the swing/linear coil, respectively, R_{Fe1} and $i_{Fe1}(t)$ are core-loss resistance and current for swing motion, respectively, and $L_{\mu 1}(t)$, $i_{\mu 1}(t)$, and $e_1(t)$ are the magnetizing inductance, current, and voltage for the swing motion, respectively. $L_{1\sigma}(\theta)$ and $M_{12\sigma}(\theta)$ are changed with θ .

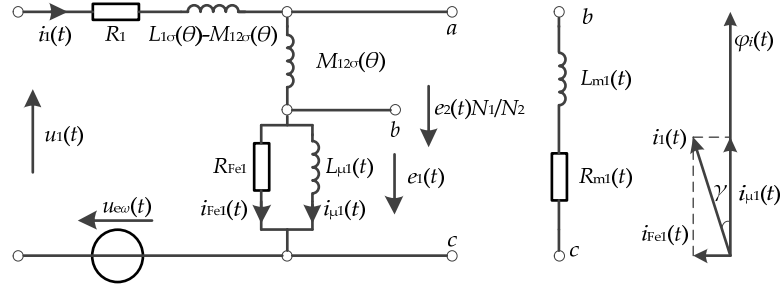


Figure 2. Equivalent circuit of swing motion.

As $i_1(t)$ is variational, the magnetic flow in the iron core $\varphi_i(t)$ is generated only by $i_{\mu 1}(t)$, and the open-circuit voltage $e_2(t)$ of the linear coil is induced by $L_{\mu 1}(t)$ and $M_{12\sigma}(\theta)$. The phase difference between $i_1(t)$ and $i_{\mu 1}(t)$ is γ . $R_{m1}(t)$ and $L_{m1}(t)$ are the excitation resistance and inductance for the swing motion, respectively, which are accorded with

$$R_{m1}(t) = 4\pi^2 f^2 R_{Fe1} L_{\mu 1}^2(t) / [R_{Fe1}^2 + 4\pi^2 f^2 L_{\mu 1}^2(t)], \quad L_{m1}(t) = R_{Fe1}^2 L_{\mu 1}(t) / [R_{Fe1}^2 + 4\pi^2 f^2 L_{\mu 1}^2(t)],$$

where f is the frequency of $i_1(t)$. The electrical time constant of the swing motion $\tau_{a1}(t)$ is equal to $[L_{1\sigma}(\theta) + L_{m1}(t)]$. Then, $\tau_{a1}(t)$ is related to R_{Fe1} , $L_{\mu 1}(t)$, and $L_{1\sigma}(\theta)$. R_{Fe1} is estimated by the analysis of iron loss. The iron yoke in the 2-DOF VCM is not laminated; its iron loss P_{Fe} consists of hysteresis loss P_h and eddy current loss P_{ec} . Considering the effect of B_m and f on P_h , P_h can be given by

$$P_h = C_h(B_m, f) f^{\alpha(B_m, f)} V B_m^{\beta(B_m, f)}, \quad (1)$$

where V is the volume of iron, and $C_h(B_m, f)$, $\alpha(B_m, f)$, and $\beta(B_m, f)$ are the coefficients of hysteresis loss, frequency, and flux density, respectively. The coefficients can be obtained by the analysis of the hysteresis curve under different flux density amplitudes. B_m is the maximum flux density of the alternating magnetic field which is excited by $i_{\mu 1}(t)$. For Equation (1), the accuracy of P_h depends on B_m greatly, and B_m is derived as follows. $e_2(t)$ is excited by $\varphi_i(t)$, and $N_1 e_2(t) / N_2 = N_1 d\varphi_i(t) / dt + M_{12\sigma}(\theta) di_1(t) / dt$. Supposing the sample period is t_0 , which is tiny, $e_2(t)$ can be described as

$$N_1 e_2(t) / N_2 = N_1 [\varphi_i(t) - \varphi_i(t - t_0)] / t_0 + M_{12\sigma} [i_1(t) - i_1(t - t_0)] / t_0, \quad (2)$$

Then, $\varphi_i(t)$ can be expressed as

$$\varphi_i(t) = \{N_1 e_2(t) t_0 - N_2 M_{12\sigma} [i_1(t) - i_1(t - t_0)]\} / (N_1 N_2) + \varphi_i(t - t_0), \quad (3)$$

where $\varphi_i(0) = \varphi_{PM}(x_j)$; $\varphi_{PM}(x_j)$ is the initial magnetic flow caused by the PM only, and its value is related with the location of linear coil x_j . $\varphi_{i\max}$ and $\varphi_{-i\max}$ are the maximum positive and negative values of $\varphi_i(t)$ in one current cycle, respectively, which are obtained by Equation (3). Considering the bias of the PM, B_m can be given by $B_m = (\varphi_{i\max} - \varphi_{-i\max}) / 2S$, where S is the cross-area of iron. Then, P_h is obtained in one period.

Based on the structure of the 2-DOF VCM, the initial magnetic flux caused by the PM to the different parts of the iron is different. This paper equally divides the iron into $2n$ parts along the main magnetic path, which is shown in Figure 3a. The width of each part is l_0 ; l_0 is tiny, and $l_0 = l / 2n$; l is the length of the main magnetic path. There are many eddy current loops within the cross-area of j th divided iron, and a supposed eddy current loop

of the area of $4rz^2$ is shown in Figure 3b, which is z away from the center line. $\varphi_i(z)$ is the magnetic flux of $4rz^2$ that is caused by $i_{\mu 1}(t)$, $r = l_{cy}/l_m$, and l_{cy} and l_m are the lengths of the iron core in directions y and z , respectively; l is the length of the iron core.

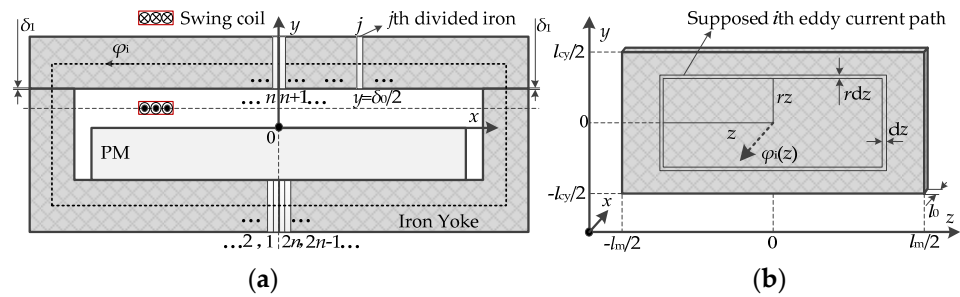


Figure 3. Analysis of eddy current loss: (a) iron is divided into n parts; (b) supposed eddy current path of j th divided iron.

The alternating magnetic density $B_i(y,z)$ of the iron core is excited by $i_{\mu 1}(t)$ within the cross-area, which is uneven. Considering the skin effect, its effective value $B_{rms}(y,z)$ can be approximately expressed as

$$B_{rms}(y,z) = B_{0rmsj} [\cosh(k_{jy}) + \cosh(k_{jz})], \quad (4)$$

where B_{0rmsj} is the effective value at the central point of j th divided iron, and

$$B_{0rmsj} = \int_{-l_m/2}^{l_m/2} \int_{-l_{cy}/2}^{l_{cy}/2} \frac{B_{rms}(y,z)}{\cosh(k_{jy}) + \cosh(k_{jz})} dydz = \frac{k_j \varphi_{irms}}{2 [l_{cy} \sinh(k_j l_m/2) + l_m \sinh(k_j l_{cy}/2)]},$$

φ_{irms} is the effective value of $\varphi_i(t)$, k_j is the skin coefficient of j th divided iron, and $k_j = \sqrt{2\pi f \mu_{rmsj} \sigma_{Fe}}$, where σ_{Fe} is the electrical conductivity of iron, and μ_{rmsj} is the magnetic conductivity of j th divided iron in one current cycle. M_{rms} can be given by $\mu_{rms} = \mu_{PMj} + f(\varphi_{irms}/S)$. $\mu = f(B)$ is the normal magnetization curve of iron, and μ_{PMj} is the initial magnetic resistance of j th divided iron that is caused by the PM. Supposing $E_{rmsj}(z)$ and $\varphi_{irmsj}(z)$ are the effective values of the induced voltage and magnetic flow of $4rz^2$, respectively, E_{irms} and φ_{irms} are the effective values of the induced voltage and magnetic flow of S , respectively. E_1 is the effective value of $e_1(t)$; then,

$$\frac{E_{rmsj}(z)}{E_{irms}} = \frac{E_{rmsj}(z)}{E_1/N_1} = \frac{\varphi_{irmsj}(z)}{\varphi_{irms}} = B_{0rmsj} \frac{4rz \sinh(k_j z) + 4z \sinh(k_j z)}{k_j \varphi_{irms}}$$

is founded, which deduces

$$E_{rmsj}(z) = 2E_1 [rz \sinh(k_j z) + z \sinh(rk_j z)] / \{N_1 [l_{cy} \sinh(k_j l_m/2) + l_m \sinh(k_j l_{cy}/2)]\}. \quad (5)$$

Referring to Figure 3b, the conductance dG corresponding to $E_{rmsj}(z)$ can be expressed as

$$dG = k_{re} \sigma_{Fe} r l_0 dz / [4(1+r^2)z], \quad (6)$$

k_{re} is the path correction coefficient, which depends on the shape and size of the cross-area of iron. Referring to Equations (5) and (6), the eddy current loss of j th divided iron P_{ecj} can be written as

$$P_{ecj} = \int_{-l_m/2}^{l_m/2} E_{rmsj}^2(z) dG = \frac{k_{re} \sigma_{Fe} r l_0 E_1^2 \int_{-l_m/2}^{l_m/2} z [rz \sinh(k_j z) + z \sinh(rk_j z)]^2 dz}{N_1^2 (1+r^2) [l_{cy} \sinh(k_j l_m/2) + l_m \sinh(k_j l_{cy}/2)]^2},$$

Then,

$$R_{Fe1} = E_1^2 / \left[C_h(B_m, f) f^{\alpha(B_m, f)} V B_m^{\beta(B_m, f)} + \sum_{j=1,2,\dots}^{2n} P_{ecj} \right]. \quad (7)$$

The estimated method for R_{Fe1} has fully considered the distribution of magnetic density; moreover, the tested E_1 is helpful in weakening the influence of non-sinusoidal current on core loss, which makes the estimated R_{Fe1} more accurate. Referring to Figure 2,

$$e_1(t) = L_{\mu 1}(t) i_{\mu 1}'(t) = N_1 e_2(t) / N_2 - M_{12\sigma} i_{\mu 1}'(t), \quad i_{\mu 1}(t) = i_1(t) - i_{Fe}(t) = i_1(t) - e_1(t) / R_{Fe1}$$

are founded, which deduce that

$$L_{\mu 1}(t) = \begin{cases} L_{\mu 1}(t - t_0) & f(\theta, t) = 0 \\ R_{Fe1} [N_1 e_2(t) / N_2 - M_{12\sigma} di_{\mu 1}(t) / dt] / f(\theta, t) & f(\theta, t) \neq 0 \end{cases} \quad (8)$$

where

$$f(\theta, t) = R_{Fe1} i_1'(t) + M_{12\sigma}'(\theta) \theta'(t) i_1'(t) + M_{12\sigma}(\theta) i_1''(t) - N_1 e_2'(t) / N_2$$

and t_0 is the sampling interval. Equation (8) indicates that $L_{\mu 1}(t)$ is an instantaneous value.

3. Estimated Method of Torque Constant

To the novel 2-DOF VCM, the torque constant C_f is the same as the back-EMF constant C_e . Due to different $x_s(t)$ and armature reaction, the gap flux density is not immobile, which leads to C_f and C_e that are variational. $X_s(t)$ is the equivalent position of the swing coil. Swing motion is integrated in linear motion, $x_s(t) = x_l + d + (d_b + b_{st} + l_{sz}/2) \sin[\theta(t)]$, which is shown in Figure 4b. x_l is the position of the linear coil, and d is the distance between the linear and swing coils as $\theta = 0$. Supposing the equivalent gap flux density of the swing motion is $B_{\delta e}[x_s(t), \varphi_i]$, and the flux through the forced edge of the swing coil is $\varphi_{\delta}[x_s(t), \varphi_i]$, $\varphi_{\delta}[x_s(t), \varphi_i] = B_{\delta}[x_s(t), \varphi_i] A_s$, and A_s is the cross-area of the swing coil on the plane xoz . The real-time torque constant $C_f[x_s(t), \varphi_i]$ can be written as

$$C_f[x_s(t), \varphi_i] = C_e[x_s(t), \varphi_i] = B_{\delta e}[x_s(t), \varphi_i] C_e[x_s(t), 0] / B_{\delta e}[x_s(t), 0], \quad (9)$$

where $C_e[x_s(t), 0]$ and $B_{\delta e}[x_s(t), 0]$ are the back-EMF constant and equivalent gap flux density at $x_s(t)$ when $\varphi_i = 0$, respectively. $C_e[x_s(t), 0]$ can be obtained by the test of back EMF. $B_{\delta e}[x_s(t), 0]$ can be obtained by the calculation or simulation of the static magnetic field.

When $\varphi_i = 0$, $\varphi_{\delta}[x_s(t), 0]$ is excited only by $F(b_s)$, $F(b_s)$ is the magnetomotive force of the PM under swing coil, and the center line of the swing coil passes through p th and q th divided iron, which are shown in Figure 4a. $\varphi_{\delta}[x_s(t), 0]$ is divided into φ_{mn} and φ_{mp} , and its equivalent magnetic circuit can be treated as Figure 4c. $R_{\delta 1}$ is the magnetic resistance of gap δ_1 ; its value is changeless and can be written as $\delta_1 / [\mu_0(l_m + \delta_1)(l_{cy} + \delta_1)]$.

$R_{mz}[x_s(t), 0]$ and $R_{my}[x_s(t), 0]$ are the magnetic resistance of iron located to the left and right of the swing coil, respectively, when $t = 0$, and

$$R_{mz}[x_s(t), 0] = \sum_{h=q, (q+1) \dots}^p I_0 / [g(B_{PMh}) S], \quad (10)$$

$$R_{my}[x_s(t), 0] = \sum_{i=1, 2 \dots}^{(q-1)} I_0 / [g(B_{PMi}) S] + \sum_{j=(p+1), (p+2) \dots}^{2n} I_0 / [g(B_{PMj}) S]. \quad (11)$$

where $\mu = g(B)$ is the initial magnetization curve, B_{PMk} is the initial flux density of k th divided iron, and k belongs to $[1 \ 2n]$. $R_{\delta 0}[x_s(t)]$ is the magnetic resistance of gap δ_0 for the swing coil at $x_s(t)$, which is hard to calculate directly. To avoid the uncertain path of magnetic field lines within gap δ_0 , this paper treats $F(b_s)$ as a constant along the x -axis, but $\varphi_{\delta}[x_s(t), 0]$ is a variate. Referring to Figure 4c,

$$R_{\delta 0}[x_s(t)] = \frac{F(b_s)}{\varphi_{\delta}[x_s(t), 0]} - \frac{\{R_{\delta 1} + R_{my}[x_s(t), 0]\} \{R_{\delta 1} + R_{mz}[x_s(t), 0]\}}{2R_{\delta 1} + R_{my}[x_s(t), 0] + R_{mz}[x_s(t), 0]}$$

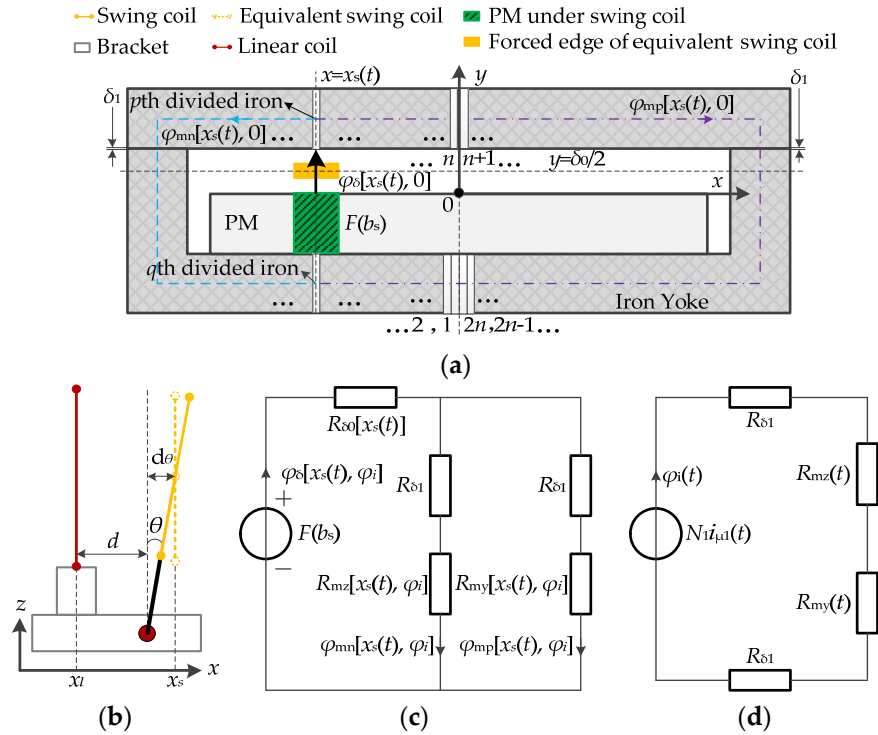


Figure 4. Analysis of armature reaction: (a) magnetic circuit of swing motion, (b) equivalent position of swing coil, (c) equivalent magnetic circuit of PM, and (d) equivalent magnetic circuit of $N_1 i_{\mu 1}(t)$.

When $i_1(t)$ is active, its equivalent magnetic circuit is as shown in Figure 4d. The added flux $\varphi_i(t)$ in iron will alter the original flux densities of divided irons, which lead to $R_{mz}[x_s(t), \varphi_i]$ and $R_{my}[x_s(t), \varphi_i]$ being changed. The variational $R_{mz}[x_s(t), \varphi_i]$ and $R_{my}[x_s(t), \varphi_i]$ cause the change in $B_{\delta}[x_s(t), \varphi_i]A_s$, so accurate $R_{mz}[x_s(t), \varphi_i]$ and $R_{my}[x_s(t), \varphi_i]$ are the key for $B_{\delta}[x_s(t), \varphi_i]$. Supposing $R_{mzr}[x_s(t), \varphi_i]$ and $R_{myr}[x_s(t), \varphi_i]$ are the magnetic resistance of iron located to the left and right of the swing coil regardless of the magnetic saturation, respectively, they can be expressed as

$$R_{mzr}[x_s(t), \varphi_i] = \left\{ \sum_{h=q, (q+1) \dots}^p l_0 / \{g(B_{PMh}) + f[\varphi_i(t)/S]\} \right\} / S,$$

$$R_{myr}[x_s(t), \varphi_i] = \sum_{i=1, 2 \dots}^{(q-1)} \frac{l_0/S}{g(B_{PMi}) + f[\varphi_i(t)/S]} + \sum_{j=(p+1), (p+2) \dots}^{2n} \frac{l_0/S}{g(B_{PMj}) + f[\varphi_i(t)/S]}.$$

In the initial magnetic path of the PM, the fluxes in 1th~nth divided irons have opposite directions to those in $(n + 1)$ th~ $2n$ th divided irons, which make $\varphi_i(t)$ magnetized in one part and demagnetized in the other part. So, only one of $R_{mzr}[x_s(t), \varphi_i]$ and $R_{myr}[x_s(t), \varphi_i]$ is affected by magnetic saturation. If $\varphi_i(t)$ has the same direction as φ_{mn} , $R_{my}[x_s(t), \varphi_i] = R_{myr}[x_s(t), \varphi_i]$; else, $R_{mz}[x_s(t), \varphi_i] = R_{mzr}[x_s(t), \varphi_i]$. Referring to Figure 4d, $R_{my}[x_s(t), \varphi_i] + R_{mz}[x_s(t), \varphi_i] = N_1^2/L_{\mu 1}(t) - 2R_{\delta 1}$ is founded. Then, $R_{mz}[x_s(t), \varphi_i]$ and $R_{my}[x_s(t), \varphi_i]$ can, respectively, be expressed as

$$R_{mz}[x_s(t), \varphi_i] = \begin{cases} R_{mzr}[x_s(t), \varphi_i] & \text{sign}[\varphi_i(t)] = \text{sign}(\varphi_{mn}) \\ N_1^2/L_{\mu 1}(t) - 2R_{\delta 1} - R_{myr}[x_s(t), \varphi_i] & \text{sign}[\varphi_i(t)] \neq \text{sign}(\varphi_{mn}) \end{cases}$$

$$R_{my}[x_s(t), \varphi_i] = \begin{cases} R_{myr}[x_s(t), \varphi_i] & \text{sign}[\varphi_i(t)] = \text{sign}(\varphi_{mn}) \\ N_1^2/L_{\mu 1}(t) - 2R_{\delta 1} - R_{mzr}[x_s(t), \varphi_i] & \text{sign}[\varphi_i(t)] \neq \text{sign}(\varphi_{mn}) \end{cases}$$

Then, $B_{\delta e}[x_s(t), \varphi_i]$ can be deduced by

$$B_{\delta e}[x_s(t), \varphi_i] = \frac{N_1^2 F(b_s)}{A_s \{L_{\mu 1}(t) \{R_{\delta 1} + R_{mz}[x_s(t), \varphi_i]\} \{R_{\delta 1} + R_{my}[x_s(t), \varphi_i]\} + N_1^2 R_{\delta 0}[x_s(t)]\}}$$

Then, $C_f[x_s(t), \varphi_i]$ and $C_e[x_s(t), \varphi_i]$ are presented.

4. Adaptive Feedforward Control Based on Estimated Electromagnetic Parameters

The proposed ACBE is a typical three-loop control system; ACR1 is the PI controller for the current loop, ASR1 is the PI controller for the speed loop, and APR1 is the P controller for the position loop, as shown in Figure 5. In particular, the parameters of ACR1, ASR1, and APR1 are changed as estimated electromagnetic parameters, which always ensure the expected performance. Further, the position feedforward controller (PFC) and drag feedforward controller (DFC) are added to the ACBE. The PFC and DFC are beneficial to tracking performance, especially as they update parameters in real time.

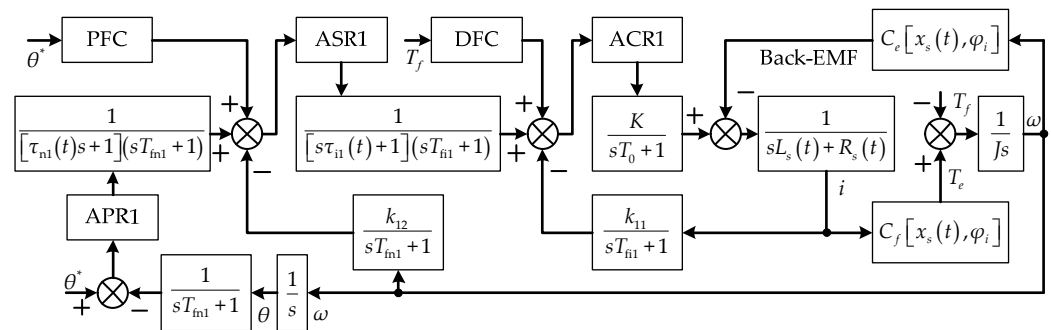


Figure 5. Schematic block diagram of ACBE upon swing motion.

In Figure 5, K and T_0 are the voltage amplification factor and equivalent time constant of the PWM converter, respectively. T_{f11} and T_{f12} are the filtering time of current feedback and position feedback, respectively. k_{11} and k_{12} are the current and speed feedback coefficients, respectively. J is the rotational inertia of the swing motion. T_e and T_f are the electromagnetic and drag torque, respectively. $w_{ACR1}(s)$, $w_{ASR1}(s)$, and $w_{APR1}(s)$ are the transfer function of ACR1, ASR1, and APR1, respectively.

$$w_{ACR1}(s) = K_{c1}(t)[1 + \tau_{i1}(t)s]/[\tau_{i1}(t)s], w_{ASR1}(s) = K_{s1}(t)[1 + \tau_{n1}(t)s]/[\tau_{n1}(t)s], w_{APR1}(s) = K_{p1}(t).$$

where $K_{c1}(t)$ and $\tau_{i1}(t)$ are the amplification coefficient and integration time constant of ACR1, respectively, $K_{s1}(t)$ and $\tau_{n1}(t)$ are the amplification coefficient and integration time constant of ASR1, respectively, and $K_{p1}(t)$ is the amplification coefficient of APR1. Ignoring the influence of speed on the bearing resistance, these variates are changed as $\tau_{a1}(t)$, $L_{m1}(t)$, $L_{1\sigma}(\theta)$, and $C_e[x_s(t), \varphi_i]$. Taking the current loop as a second-order system, based on the traditional performance optimization tuning method,

$$K_{c1}(t) = [L_{1\sigma}(\theta) + L_{m1}(t)]/[2K(T_0 + T_{f11})k_{11}], \tau_{i1}(t) = \tau_{a1}(t) = [L_{1\sigma}(\theta) + L_{m1}(t)]/[R_1 + R_{m1}(t)].$$

Which indicates that the parameters of $w_{ACR1}(s)$ are changed as $\tau_{a1}(t)$, $L_{m1}(t)$, and $L_{1\sigma}(\theta)$ and always keep the performance of the current loop. Considering back EMF, the open-loop transfer function of current-loop $W_{oc}(s)$ can be written as

$$W_{oc}(s) = K_{c1}(t)k_{11}[1 + \tau_{i1}(t)]/\left\{\tau_{i1}(t)(T_0s + 1)(T_{f11}s + 1)\left\{L_s(t)s^2 + R_s(t)s + C_e^2[x_s(t), \varphi_i]/J\right\}\right\}. \quad (12)$$

In order to reduce the impact of bearing resistance on the tracking performance, the DFC is added at the input of the current loop. The transfer function of the DFC is $F_n(s)$, and

$$F_n(s) = k_{11}[1 + W_{oc}(s)] / \left\{ W_{oc}(s)(T_{f11}s + 1)C_f[x_s(t), \varphi_i] \right\},$$

which indicates that the parameters of $F_n(s)$ are changed as $\tau_{i1}(t)$, $K_{c1}(t)$, and $C_e[x_s(t), \varphi_i]$ and effectively keep the accuracy of the DFC. A filter link is added after ASR1, and the current loop is treated as an inertia link; then, the open-loop transfer function of the speed-loop $W_{os}(s)$ can be written as

$$W_{os}(s) = C_f[x_s(t), \varphi_i]K_{s1}(t)k_{12}[1 + \tau_{n1}(t)s] / \left\{ Jk_{11}\tau_{n1}(t)s^2[T_e(t)s + 1] \right\}, \quad (13)$$

where $T_e(t)$ is the equivalent time constant of the current loop. Referring to Equation (12) and omitting the higher term of the small time constant,

$$T_e(t) = L_s(t) / [R_s(t) + K_{c1}(t)k_{11}] + \tau_{i1}(t)[R_s(t) + K_{c1}(t)k_{11}] / [K_{c1}(t)k_{11}] + T_{f11}.$$

Equation (13) indicates that $W_{os}(s)$ is a typical type II system. Supposing h is the intermediate frequency width of the speed loop, $K_{s1}(t)$ and $\tau_{n1}(t)$ can be deduced as

$$\tau_{n1}(t) = hT_e(t), K_{s1}(t) = Jk_{11} / \left\{ \sqrt{h}T_e(t)C_f[x_s(t), \varphi_i]k_{12} \right\},$$

which indicates that the parameters of $w_{ASR1}(s)$ are changed as $L_{m1}(t)$, $L_{1\sigma}(\theta)$, $\tau_{i1}(t)$, $K_{c1}(t)$, h , and $C_f[x_s(t), \varphi_i]$ and always keep the performance of the speed loop. In order to further improve the track performance of the speed loop, the PFC is added at the input of the speed loop. The transfer function of the PFC is $F_r(s)$, and

$$F_r(s) = k_{12}[W_{oc}(s) + 1] / [W_{oc}(s)(sT_{f11} + 1)].$$

Supposing the gain of the speed loop is $K_{os}(t)$,

$$K_{os}(t) = K_{s1}(t)k_{12}C_f[x_s(t), \varphi_i] / [JhT_e(t)k_{11}].$$

Referring to Figure 5, the close-loop transfer function of position-loop $W_{cp}(s)$ can be written as

$$W_{cp}(s) = K_{p1}(t)K_{os}(t) / \left\{ k_{12} \left[T_e(t)s^4 + s^3 + K_{os}(t)\tau_{n1}(t)s^2 + K_{os}(t)s \right] + K_{p1}(t)K_{os}(t) \right\} \\ \approx K_{p1}(t) / \left\{ k_{12} \left\{ \tau_{n1}(t) + T_e(t) + 1 / [K_{os}(t)\tau_{n1}(t)] \right\} + k_{12}s + K_{p1}(t) \right\},$$

which is treated as a second-order system. Supposing the damping ratio is ζ , and the undamped natural frequency is ω_n , then

$$2\zeta\omega_n = 1 / \left\{ \tau_{n1}(t) + T_e(t) + 1 / [K_{os}(t)\tau_{n1}(t)] \right\}, \omega_n^2 = K_{p1}(t) / \left\{ k_{12} \left\{ \tau_{n1}(t) + T_e(t) + 1 / [K_{os}(t)\tau_{n1}(t)] \right\} \right\}$$

is founded, which deduces

$$K_{p1}(t) = k_{12} / \left\{ 4\zeta^2 \left\{ \tau_{n1}(t) + T_e(t) + 1 / [K_{os}(t)\tau_{n1}(t)] \right\} \right\}.$$

The above expositions show that the control parameters of ACBE are changed as estimated electromagnetic parameters from the inside out; once the estimated electromagnetic parameters are accurate, the expected tracking performance can be realized.

5. Experimental Test and Discussion

Based on the proposed control model, an experimental platform was conducted, as shown in Figure 6.

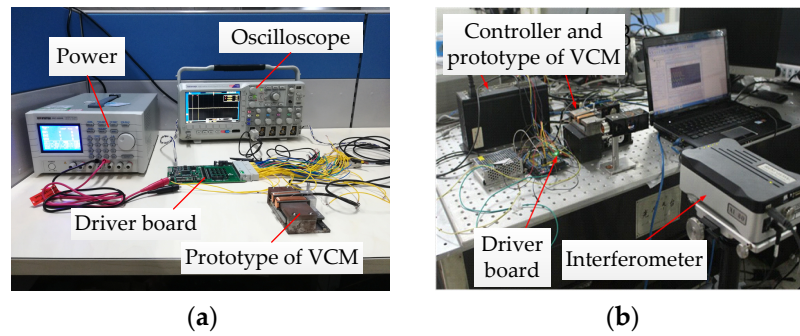


Figure 6. Experimental platform: (a) parameter test and (b) performance test.

The permeability of the core is always changed by the variational current. Figure 7a is the input current of the swing coil, and the tested curve of $e_2(t)$ is shown in Figure 7b. The phase between $i_1(t)$ and $e_2(t)$ is not 90 degrees due to $R_{m1}(t)$. Based on the tested $e_2(t)$ and Equation (7), $R_{Fe1} = 0.166 \Omega$ is obtained in this cycle. Then, the estimated $\tau_{a1}(t)$ is deduced by the proposed method, which is shown in Figure 7c. The estimated $\tau_{a1}(t)$ indicates that the electrical time constant of the swing coil has changed greatly within a cycle of $i_1(t) = 1.4\sin(2\pi t)$, and it is significant to estimate the electrical time constant and update the related control parameters. Due to the hysteresis characteristic of the core, $\tau_{a1}(t)$ lags behind $i_1(t)$ obviously. When the absolute value of $i_1(t)$ is greater than 1A, $\tau_{a1}(t)$ has less change due to the core being saturated.

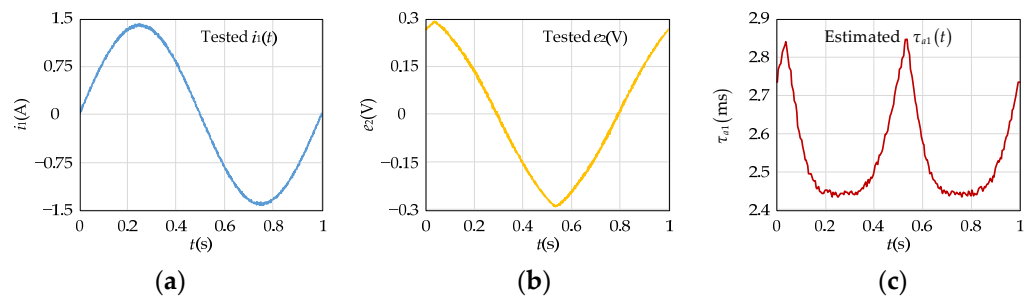


Figure 7. Variation in electrical time constant $\tau_{a1}(t)$ in one cycle under $i_1(t) = 1.4\sin(2\pi t)$: (a) curve of tested $i_1(t)$, (b) curve of tested $e_2(t)$, and (c) curve of estimated $\tau_{a1}(t)$ by proposed method.

The accuracy of the estimated $\tau_{a1}(t)$ is important for the performance of the proposed ACBE, but both the amplitude and frequency of $i_1(t)$ can affect the estimated accuracy. Figure 8 shows the effect of different current amplitudes on the accuracy of the estimated $\tau_{a1}(t)$. Due to the increasing B_m and core reluctance, the estimated R_{Fe1} increases slightly as the current amplitude increases, but the estimated $L_{\mu 1e}$ decreases, which is shown in Figure 8a,b. $L_{\mu 1e}$ is the effective value of $L_{\mu 1}(t)$. The tested R_s and L_s in Figure 8c,d are obtained by the digital electric bridge, and the estimated R_s and L_s are deduced by the estimated R_{Fe1} and $L_{\mu 1e}$. In comparison with the tested R_s and L_s , the estimated values are smaller due to the accuracy of the estimated R_{Fe1} being related to the tested error of $e_2(t)$ and the estimated error of the core loss. The effective value of noise of $e_2(t)$ has a greater proportion as the value of E_2 is smaller, which makes the error of the estimated R_{Fe1} larger at a lower current, and the accuracy of the estimated R_s and L_s increases as I changes from 0.1 A to 1 A. When I exceeds 1 A, the core becomes saturated, and the estimated core loss based on the proposed method is relatively bigger than that when it is not saturated, which leads to a slightly smaller estimated R_{Fe1} . The value of the estimated $L_{\mu 1}(t)$ is related to the estimated R_{Fe1} ; thus, the variation tendency of $L_{\mu 1}(t)$ is similar to that of R_{Fe1} . So, the estimated R_s and L_s have the highest accuracy around $I = 1$ A. Based on Figure 8c,d, Figure 8e shows that the highest accuracy of the estimated electrical time constants under the proposed method is around 1.31%, which appears at the saturation point of the core.

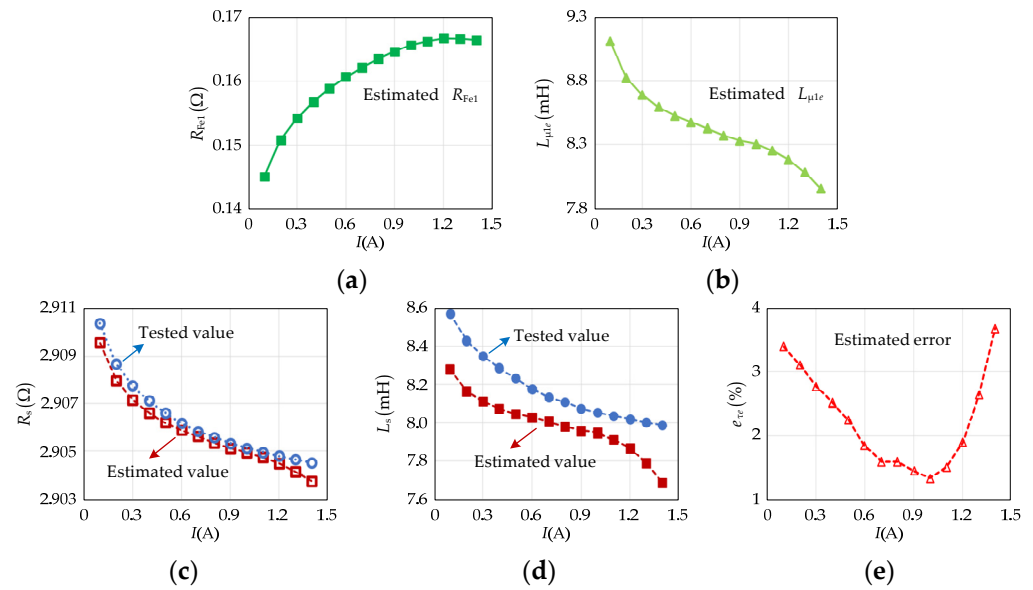


Figure 8. Accuracy of estimated $\tau_{a1}(t)$ vs. different amplitudes of $i_1(t) = I\sin(2\pi t)$: (a) the value of estimated R_{Fe1} , (b) the value of estimated $L_{\mu1e}$, (c) the value of estimated and tested R_s , (d) the value of estimated and tested L_s , and (e) estimated error of τ_{a1} .

Figure 9 shows the effect of different current frequencies on the accuracy of the estimated $\tau_{a1}(t)$. Due to the increasing f , the estimated R_{Fe1} increases obviously with the increase in current frequency, but the estimated $L_{\mu1e}$ also decreases, which is shown in Figure 9a,b. The accuracy of the estimated core loss is depressed with the rise in current frequency, which leads to the accuracy of the estimated R_{Fe1} decreasing gradually. The variation tendency of $L_{\mu1}(t)$ is also similar to that of R_{Fe1} . So, the estimated R_s and L_s are smaller than the tested R_s and L_s , and the estimation accuracy decreases with increasing frequency, which is shown in Figures 9c and 9d, respectively. Figure 9e shows that the estimation accuracy of the electrical time constants also decreases with increasing frequency, which is from 1.31% to 2.02% as f goes from 1 Hz to 10 Hz.

Figures 8 and 9 illustrate that the electrical time constant estimation based on the proposed method has high accuracy around the saturation point of the core and decreases with increasing frequency.

Figure 10a,b show the palstance ω and armature voltage E_{bEMF} of the back-EMF test, respectively. The tested static C_f is obtained by E_{bEMF}/ω , which is shown in Figure 10c. Due to the effective length of the swing coil being increased as $\cos(\theta)$ becomes smaller, the static C_f has minimum and maximum values of around $\theta = 0^\circ$ and $\theta = \pm 8^\circ$, respectively, which are 28.356 mN/A and 28.905 mN/A. The armature current can enhance or reduce the magnetic density of the air gap. When $I = 1$ A, the tested dynamic C_f for size 0.5° within $[-8^\circ, 8^\circ]$ is shown in Figure 10d. Compared to the static C_f , the dynamic C_f under $I = 1$ A is larger and also has minimum and maximum values of around $\theta = 0^\circ$ and $\theta = \pm 8^\circ$, respectively. Without the proposed method, the error of C_f under $I = 1$ A is around 4.6%, which is shown in Figure 10e. Figure 10d shows that the estimated dynamic C_f is smaller than the tested value because the estimated $L_{u1}(t)$ is smaller than the actual value. The estimated accuracy is reduced as $\cos(\theta)$ becomes smaller because the difference between R_{mz} and R_{my} becomes bigger as $\cos(\theta)$ becomes smaller. Figure 10e shows that the error of C_f under $I = 1$ A with the proposed method is around 1.5%.

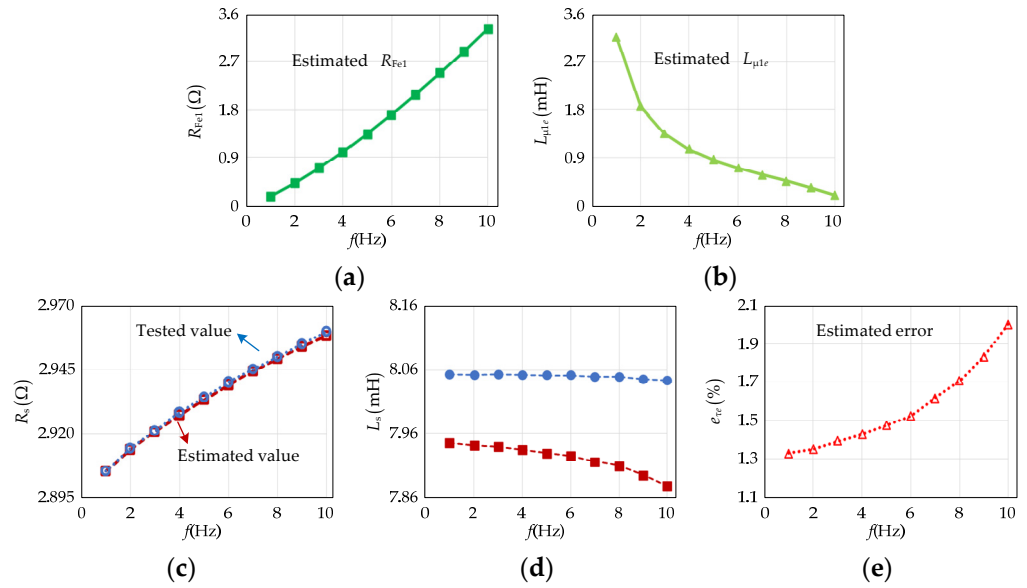


Figure 9. Accuracy of estimated $\tau_{a1}(t)$ vs. different frequency of $i_1(t) = \sin(2\pi ft)$: (a) the value of estimated R_{Fe1} , (b) the value of estimated $L_{\mu 1e}$, (c) the value of estimated and tested R_s , (d) the value of estimated and tested L_s , and (e) estimated error of τ_{a1} .

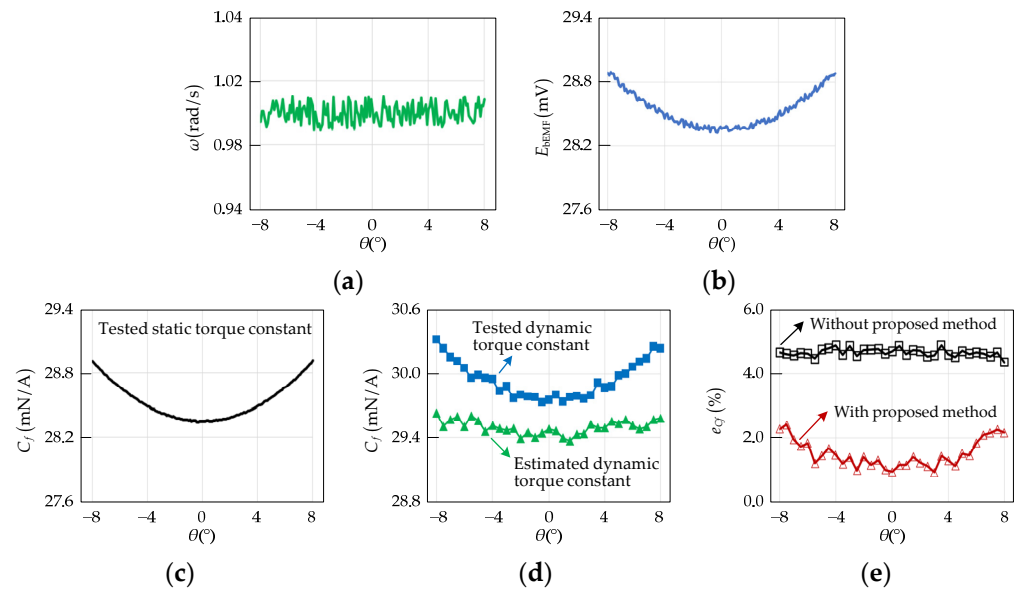


Figure 10. Accuracy of estimated C_f under proposed method: (a) palstance curve of back-EMF test, (b) armature voltage curve of back-EMF test, (c) curve of tested static torque constant, (d) tested and estimated dynamic torque constant under $I = 1$ A, and (e) error of estimated torque constant under proposed method under $I = 1$ A.

In order to verify the track performance of ACBE, this paper takes fuzzy control (FZC) as a comparative object. The given angle and palstance input of reciprocating motion are shown in Figures 11a and 11b, respectively; the angle is from -8° to $+8^\circ$, $f = 1$ Hz, and palstance is 0.698 rad/s at uniform motion. Under the given input, Figure 11c shows the current of the swing coil with ACBE and FZC; I_u is the current at uniform motion, which is around 1 A. The magnitude and fluctuation of the armature current can affect the accuracy of the control parameters of ACBE and vice versa. The control parameters of ACBE have higher accuracy when $I_u = 1$ A and $f = 1$ Hz, which make its current fluctuations lower than those of FZC. The varying torque (acceleration) will increase the amplitude of the armature current, which is not beneficial to the tracking performance of ACBE.

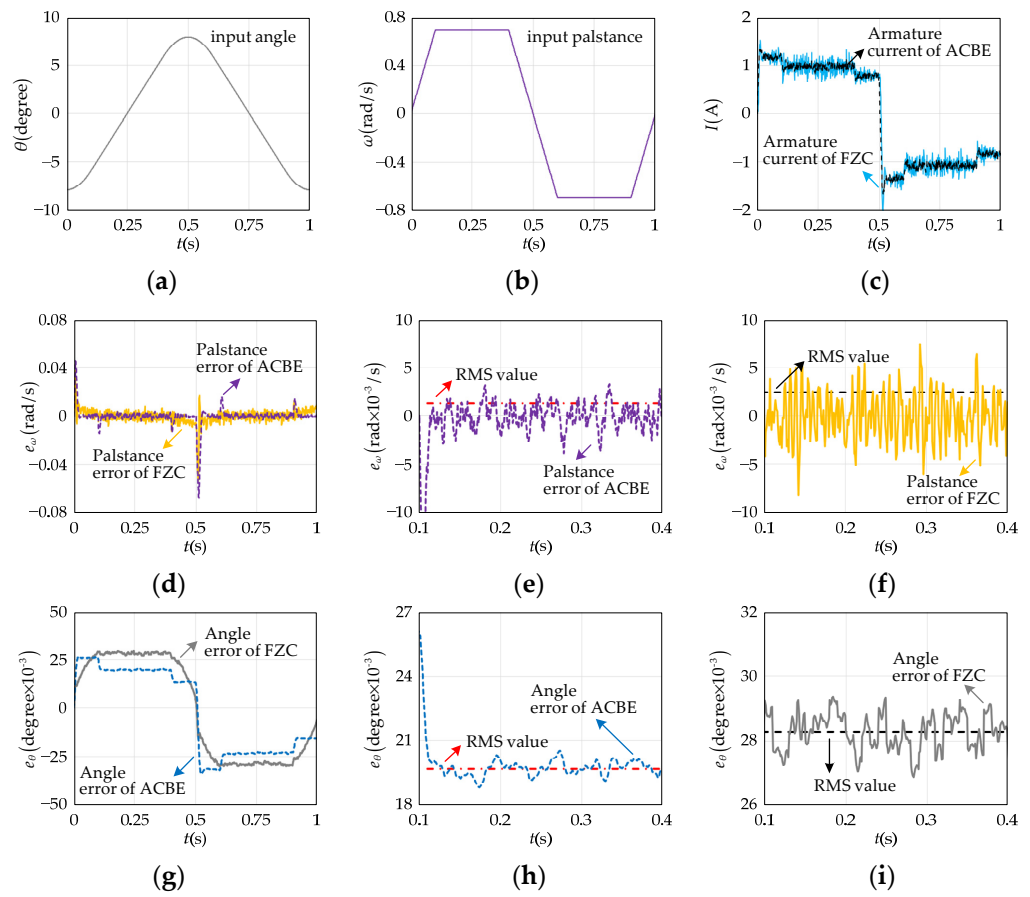


Figure 11. Tracking performance of reciprocating motion (angle is from -8° to $+8^\circ$ and $f = 1$ Hz) under ACBE and FZC: (a) angle input of reciprocating motion, (b) palstance input of reciprocating motion, (c) armature current of ACBE and FZC, (d) palstance track error of ACBE and FZC, (e) palstance track error of ACBE and its RMS value at uniform motion, (f) palstance track error of FZC and its RMS value at uniform motion, (g) angle track error of ACBE and FZC, (h) angle track error of ACBE and its RMS value at uniform motion, and (i) angle track error of FZC and its RMS value at uniform motion.

Figure 11d shows that the track error of palstance $e_\omega(t)$ under ACBE is larger than that of FZC as the torque changes (acceleration) but lower in the region of uniform motion. Under the given input of palstance, the region of uniform motion of ACBE and FZC means the steady-state region of the response curve of palstance, which is also called effective travel. The effective travel of ACBE is around 11.687° , which is lesser than that of FZC (12°). Within the region of uniform motion, the palstance track performance of ACBE is better than that of FZC, which is shown in Figure 11e,f. The palstance track error at uniform motion of ACBE is less than 4×10^{-3} rad/s, and that of FZC is 7.5×10^{-3} rad/s. The root-mean-square (RMS) of the palstance track error can partly reflect the palstance track performance of the control method at uniform motion, where ACBE is around 1.3×10^{-3} rad/s and FZC is around 2.5×10^{-3} rad/s. Similar to the palstance track error, Figure 11g shows that the track error of angle $e_\theta(t)$ under ACBE is more than that of FZC at the beginning of motion and lesser at uniform motion. Within the region of uniform motion, the $e_\theta(t)$ of ACBE is changed from 18.8×10^{-3} degrees to 20.5×10^{-3} degrees, and its RMS value is 19.7×10^{-3} degrees, which is shown in Figure 11h. Meanwhile, the $e_\theta(t)$ of FZC is changed from 26.9×10^{-3} degrees to 29.3×10^{-3} degrees, and its RMS value is 28.3×10^{-3} degrees, which is shown in Figure 11i. Figure 11 reveals that ACBE with higher accuracy control parameters has better track performance than FZC at the region of uniform motion but lesser effective travel. Both the armature current and reciprocating frequency can affect the accuracy of the control parameters of ACBE.

I_u is the armature current at uniform motion, which can be increased by adjusting the friction torque. Different I_u changes the accuracy of the control parameters of ACBE, which determine the tracking performance of ACBE. θ_e is effective travel, and $e_{\omega\text{RMS}}$ and $e_{\theta\text{RMS}}$ are the RMS values of $e_{\omega}(t)$ and $e_{\theta}(t)$ at uniform motion, respectively, which are evaluating indicators of tracking performance. Figure 12 shows the impact of different I_u on the θ_e , $e_{\omega\text{RMS}}$, and $e_{\theta\text{RMS}}$ of ACBE and FZC. When I_u is changed from 0.4 A to 1.2 A (step size 0.1 A), the θ_e of FZC is always a constant, the $e_{\omega\text{RMS}}$ of FZC hardly changes, and the $e_{\theta\text{RMS}}$ of FZC is changed from 25.7×10^{-3} degrees to 28.9×10^{-3} degrees as the I_u increases. For ACBE, the θ_e , $e_{\omega\text{RMS}}$, and $e_{\theta\text{RMS}}$ have a similar change trend as the increase in I_u ; their best points are all around $I_u = 1$ A, which is the critical saturation point of the iron core. When ACBE works at the critical saturation point of the iron core, its parameters have the least fluctuation. The values of I_u not only determine the accuracy of the ACBE parameters at the uniform motion but also at the acceleration motion. When the armature current is closer to 1 A, the accuracy of ACBE parameters is higher. Compared to FZC, ACBE is more affected by the change in armature current, but within $I_u = [0.8 \text{ A } 1 \text{ A}]$, the tracking performance of ACBE is better than that of FZC, especially when I_u is around 1 A.

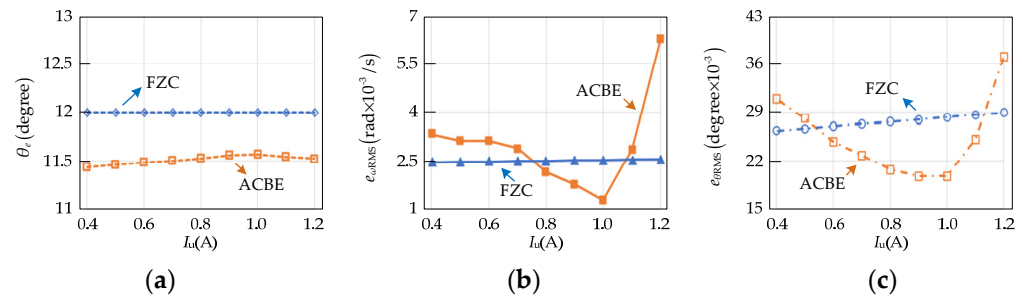


Figure 12. Track performance of reciprocating motion (angle is from -8° to $+8^\circ$ and $f = 1$ Hz) under ACBE and FZC with different I_u : (a) effective travel, (b) RMS value of $e_{\omega}(t)$ at uniform motion, and (c) RMS value of $e_{\theta}(t)$ at uniform motion.

Except for the armature current, the reciprocating frequency f also can affect the accuracy of the control parameters of ACBE. The angle range of the reciprocating motion is kept at -8° to $+8^\circ$, and I_u is around 1 A. Figure 13 shows the impact of different f on the θ_e , $e_{\omega\text{RMS}}$, and $e_{\theta\text{RMS}}$ of ACBE and FZC. As f increases, the acceleration and amplitude of the given palstance curve (trapezoidal wave) become bigger, which increases the armature current at acceleration motion and the displacement at the sampling interval. So, the tracking performance of ACBE and FZC declines as f increases. An increased armature current seriously degrades the accuracy of the control parameters of ACBE at acceleration motion; the θ_e of ACBE decreases more than that of FZC as f increases, which is shown in Figure 13a. At uniform motion, increased f also reduces the accuracy of the control parameters of ACBE. The $e_{\theta\text{RMS}}$ and $e_{\omega\text{RMS}}$ of ACBE are more than those of FZC when f exceed 3 Hz and 4 Hz, respectively, which is shown in Figure 13b,c. ACBE is more affected as f increases, but within $f = 3$ Hz, the tracking performance of ACBE is still better than that of FZC.

The above experiments show that the proposed methods for MEPs have higher accuracy at low frequency and around the critical saturation point of the iron core. The tracking performance of ACBE depends on the accuracy of the estimated electromagnetic parameters.

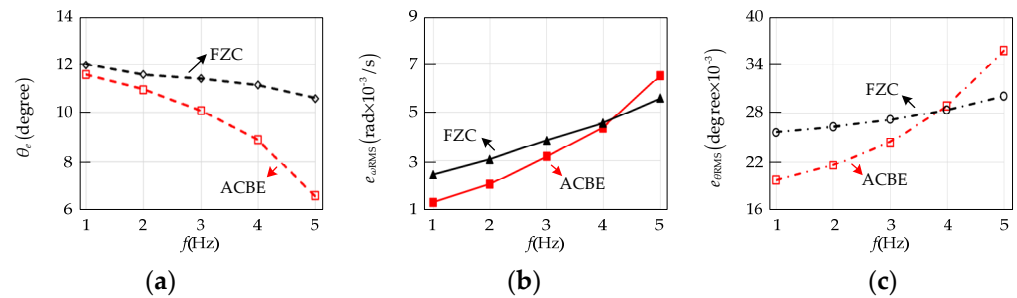


Figure 13. Track performance of reciprocating motion (angle is from -8° to $+8^{\circ}$ and $I_u = 1$ A) under ACBE and FZC with different f : (a) effective travel, (b) RMS value of $e_{\omega}(t)$ at uniform motion, and (c) RMS value of $e_{\theta}(t)$ at uniform motion.

6. Conclusions

In this paper, through the analysis of the armature current and the flux of the main magnetic circuit, the real-time armature inductance, the reluctance of the main magnetic circuit, and the air-gap magnetic density are deduced. Further, the electromagnetic parameters are estimated. According to the estimated electromagnetic parameters, ACBE adjusts the control parameters of the current loop, speed loop, position loop, and feedforward controller from inside out. A higher accuracy of the estimated electromagnetic parameters and better tracking performance of ACBE are observed. With the proposed method, the palstance tracking error of the swing motion is within 4×10^{-3} rad/s, and the angle tracking error is around 19.7×10^{-3} degrees. This study indicates that adaptive algorithms based on a real-time control model have better tracking performance at uniform motion in a motor system. In addition, ACBE can not only be adopted in the two-DOF VCM but can also be used in other linear VCMs which need just one detective coil, which means that the proposed ACBE can be applied more widely.

Author Contributions: Z.Y. and M.L. contributed to this research article in the formal analysis, investigation, resources, data curation, and writing of the original draft. J.-a.D. contributed to the conceptualization and methodology of this research article. Y.J. contributed to the writing expression of this research article. All authors have read and agreed to the published version of the manuscript.

Funding: This research was funded by the National Natural Science Foundation of China, grant number 52377048, the Natural Science Foundation of Hunan Province of China under Grant 2022JJ30138, and the Natural Science Foundation of Hunan Province of China under Grant 2023JJ30159.

Data Availability Statement: The data presented in this study are available on request from the corresponding author due to privacy.

Conflicts of Interest: The authors declare no conflicts of interest.

References

- Peng, G.; Yang, C.; He, W.; Chen, C.P. Force Sensorless Admittance Control with Neural Learning for Robots with Actuator Saturation. *IEEE Trans. Ind. Electron.* **2020**, *67*, 3138–3148. [\[CrossRef\]](#)
- Jang, N.; Ihn, Y.S.; Choi, N.; Gu, G.; Jeong, J.; Yang, S.; Yim, S.; Kim, K.; Oh, S.R.; Hwang, D. Compact and Lightweight End-Effectors to Drive Hand-Operated Surgical Instruments for Robot-Assisted Microsurgery. *IEEE/ASME Trans. Mechatron.* **2020**, *25*, 1933–1943. [\[CrossRef\]](#)
- Motzki, P.; Khelifa, F.; Zimmer, L.; Schmidt, M.; Seelecke, S. Design and Validation of a Reconfigurable Robotic End-Effector Based on Shape Memory Alloys. *IEEE/ASME Trans. Mechatron.* **2019**, *24*, 293–303. [\[CrossRef\]](#)
- Liang, C.; Wang, F.; Huo, Z.; Shi, B.; Tian, Y.; Zhao, X.; Zhang, D. A 2-DOF Monolithic Compliant Rotation Platform Driven by Piezoelectric Actuators. *IEEE Trans. Ind. Electron.* **2020**, *67*, 6963–6974. [\[CrossRef\]](#)
- Cheng, C.H.; Hung, S.K. A piezoelectric two-degree-of-freedom nanostepping motor with parallel design. *IEEE/ASME Trans. Mechatron.* **2018**, *21*, 2197–2199. [\[CrossRef\]](#)
- Zhang, Z.; Luo, M.; Zhou, H.; Duan, J.A. Design and analysis of a novel two-degree-of-freedom voice coil motor. *IEEE/ASME Trans. Mechatron.* **2019**, *24*, 2908–2918. [\[CrossRef\]](#)
- Shi, Y.; Zhang, J.; Lin, Y.; Wu, W. Improvement of Low-Speed Precision Control of a Butterfly-Shaped Linear Ultrasonic Motor. *IEEE Access* **2020**, *8*, 135131–135137. [\[CrossRef\]](#)

8. Li, P.; Li, P.; Sui, Y. Adaptive Fuzzy Hysteresis Internal Model Tracking Control of Piezoelectric Actuators with Nanoscale Application. *IEEE Trans. Fuzzy Syst.* **2015**, *24*, 1246–1254. [[CrossRef](#)]
9. Cheng, L.; Liu, W.; Hou, Z.G.; Huang, T.; Yu, J.; Tan, M. An Adaptive Takagi–Sugeno Fuzzy Model-Based Predictive Controller for Piezoelectric Actuators. *IEEE Trans. Ind. Electron.* **2017**, *64*, 3048–3058. [[CrossRef](#)]
10. Chen, S.Y.; Chiang, H.H.; Liu, T.S.; Chang, C.H. Precision Motion Control of Permanent Magnet Linear Synchronous Motors Using Adaptive Fuzzy Fractional-Order Sliding-Mode Control. *IEEE/ASME Trans. Mechatron.* **2019**, *24*, 741–752. [[CrossRef](#)]
11. Pan, H.; Sun, W.; Gao, H.; Jing, X. Disturbance Observer-Based Adaptive Tracking Control with Actuator Saturation and Its Application. *IEEE Trans. Autom. Sci. Eng.* **2016**, *13*, 868–875. [[CrossRef](#)]
12. Liu, X.; Cao, H.; Wei, W.; Wu, J.; Li, B.; Huang, Y. A Practical Precision Control Method Base on Linear Extended State Observer and Friction Feedforward of Permanent Magnet Linear Synchronous Motor. *IEEE Access* **2020**, *8*, 68226–68238. [[CrossRef](#)]
13. Cho, K.; Kim, J.; Choi, S.B.; Oh, S. A High-Precision Motion Control Based on a Periodic Adaptive Disturbance Observer in a PMLSM. *IEEE/ASME Trans. Mechatron.* **2014**, *20*, 2158–2171. [[CrossRef](#)]
14. Zhao, L.; Zhang, B.; Yang, H.; Wang, Y. Observer-Based Integral Sliding Mode Tracking Control for a Pneumatic Cylinder with Varying Loads. *IEEE Trans. Syst. Man Cybern. Syst.* **2020**, *50*, 2650–2658. [[CrossRef](#)]
15. Liu, Y.; Gao, J.; Zhong, Y.; Zhang, L. Extended State Observer-Based IMC-PID Tracking Control of PMLSM Servo Systems. *IEEE Access* **2021**, *9*, 49036–49046. [[CrossRef](#)]
16. Lu, W.; Tang, B.; Ji, K.; Lu, K.; Wang, D.; Yu, Z. A New Load Adaptive Identification Method Based on an Improved Sliding Mode Observer for PMSM Position Servo System. *IEEE Trans. Power Electron.* **2020**, *36*, 3211–3223. [[CrossRef](#)]
17. Humaidi, A.J.; Badr, H.M.; Hameed, A.H. PSO-Based Active Disturbance Rejection Control for Position Control of Magnetic Levitation System. In Proceedings of the 2018 5th International Conference on Control, Decision and Information Technologies (CoDIT), Thessaloniki, Greece, 10–13 April 2018.
18. Niu, S.; Luo, Y.; Fu, W.; Zhang, X. Robust Model Predictive Control for a Three-Phase PMSM Motor with Improved Control Precision. *IEEE Trans. Ind. Electron.* **2020**, *68*, 838–849. [[CrossRef](#)]
19. Xie, S.; Ren, J. Linearization of Recurrent-Neural-Network-Based Models for Predictive Control of Nano-Positioning Systems Using Data-Driven Koopman Operators. *IEEE Access* **2020**, *8*, 147077–147088. [[CrossRef](#)]
20. Xu, Q. Digital Integral Terminal Sliding Mode Predictive Control of Piezoelectric-Driven Motion System. *IEEE Trans. Ind. Electron.* **2016**, *63*, 3976–3984. [[CrossRef](#)]
21. Shi, S.; Guo, L.; Chang, Z.; Zhao, C.; Chen, P. Current Controller Based on Active Disturbance Rejection Control with Parameter Identification for PMSM Servo Systems. *IEEE Access* **2023**, *11*, 46882–46891. [[CrossRef](#)]
22. Wang, Z.; Chai, J.; Xiang, X.; Sun, X.; Lu, H. A Novel Online Parameter Identification Algorithm Designed for Deadbeat Current Control of the Permanent-Magnet Synchronous Motor. *IEEE Trans. Ind. Appl.* **2022**, *58*, 2029–2041. [[CrossRef](#)]
23. Lian, C.; Xiao, F.; Liu, J.; Gao, S. Parameter and VSI Nonlinearity Hybrid Estimation for PMSM Drives Based on Recursive Least Square. *IEEE Trans. Transp. Electrification* **2023**, *9*, 2195–2206. [[CrossRef](#)]
24. Brosch, A.; Wallscheid, O.; Böcker, J. Long-Term Memory Recursive Least Squares Online Identification of Highly Utilized Permanent Magnet Synchronous Motors for Finite-Control-Set Model Predictive Control. *IEEE Trans. Power Electron.* **2023**, *38*, 1451–1467. [[CrossRef](#)]
25. AHmed, H.M.; Jlassi, I.; Cardoso, A.J.M.; Bentaallah, A. Model-Free Predictive Current Control of Synchronous Reluctance Motors Based on a Recurrent Neural Network. *IEEE Trans. Ind. Electron.* **2022**, *69*, 10984–10992.
26. Deng, W.; Qian, Z.; Chen, W.; Qian, C.; Wang, Q. Orthotropic Material Parameters Identification Method of Stator Core and Windings in Electric Motors. *IEEE Trans. Energy Convers.* **2023**, *38*, 2464–2474. [[CrossRef](#)]

Disclaimer/Publisher’s Note: The statements, opinions and data contained in all publications are solely those of the individual author(s) and contributor(s) and not of MDPI and/or the editor(s). MDPI and/or the editor(s) disclaim responsibility for any injury to people or property resulting from any ideas, methods, instructions or products referred to in the content.